






Toward a Standard Approach for UAS-Based Multiangular Dataset Collection for BRDF Analysis

Ilaria Petracca , *Member, IEEE*, Daniele Latini , Marco Di Giacomo , Fabrizio Niro, Stefania Bonafoni , *Senior Member, IEEE*, and Fabio Del Frate , *Senior Member, IEEE*

Abstract—In this work, we address the bidirectional reflectance distribution function (BRDF) characterization of homogeneous surfaces by means of multiangular datasets acquired with an unmanned aerial system (UAS) carrying a multispectral sensor (MAIA) replicating the spectral characteristics of the multispectral instrument onboard Copernicus Sentinel-2 satellite. The UAS field campaign was performed in clear-sky conditions over two different test sites, a vegetation cover and an asphalted area, exhibiting different behaviors in terms of surface reflectance anisotropy. A dual angular approach for the processing of the reflectance measurements is examined: a conical configuration considering a cone angle of 10° (hemispherical conical-reflectance distribution) and a directional configuration (hemispherical directional-reflectance distribution) considering a cone angle of 3° . Afterward, the retrieval of the parameters of the Ross–Li–Maignan BRDF model was implemented by a least-squared fitting of the UAS reflectance measurements for each MAIA band. The accuracy of the modeled reflectances was evaluated and the overall relative root-mean-square error between the measured and modeled reflectances was less than 10% for both test sites. The outcomes of the present study go toward the definition of a standard approach for UAS-based measurements with high angular resolution features for BRDF modeling, avoiding the well-known issues related to the use of ground-based and satellite-based instruments, and proving the UAS effectiveness in supporting calibration and validation activities of satellite missions.

Index Terms—Bidirectional reflectance distribution function (BRDF), multiangular acquisition, surface reflectance anisotropy, unmanned aerial system (UAS).

Received 18 October 2023; revised 11 February 2024 and 9 September 2024; accepted 14 October 2024. Date of publication 17 October 2024; date of current version 6 November 2024. (Corresponding author: Ilaria Petracca.)

Ilaria Petracca is with GEO-K S.r.l., Via del Politecnico 1, 00133 Rome, Italy, and also with the Department of Civil Engineering and Computer Science Engineering, Tor Vergata University of Rome, Via del Politecnico 1, 00133 Rome, Italy (e-mail: ilaria.petracca@uniroma2.it).

Daniele Latini is with GEO-K S.r.l., Via del Politecnico 1, 00133 Rome, Italy (e-mail: daniele.latini@geo-k.co).

Marco Di Giacomo is with GEO-K S.r.l., Via del Politecnico 1, 00133 Rome, Italy, and also with the Department of Civil Engineering and Computer Science Engineering, Tor Vergata University of Rome, Via del Politecnico 1, 00133 Rome, Italy (e-mail: Marco.Di.Giacomo@uniroma2.it).

Fabrizio Niro is with the SERCO for European Space Agency (ESA/ESRIN), Largo Galileo Galilei 1, 00044 Frascati (RM), Italy (e-mail: fabrizio.niro@ext.esa.int).

Stefania Bonafoni is with the Department of Engineering, University of Perugia, Via G. Duranti 93, 06125 Perugia, Italy (e-mail: stefania.bonafoni@unipg.it).

Fabio Del Frate is with the Department of Civil Engineering and Computer Science Engineering, Tor Vergata University of Rome, Via del Politecnico 1, 00133 Rome, Italy (e-mail: fabio.del.frate@uniroma2.it).

Digital Object Identifier 10.1109/JSTARS.2024.3482577

I. INTRODUCTION

MOST natural surfaces show reflective anisotropic characteristics, i.e., they are non-Lambertian even if the surface type is homogeneous. They reflect electromagnetic radiation in different ways and different amounts depending on viewing and illumination conditions and reflective features of the surface. Such behavior depends on the level of anisotropy of the surface itself that can be quantitatively described by the bidirectional reflectance distribution function (BRDF) [1]. BRDF has received increasing attention over the years in advanced satellite data analysis for the albedo computation [2], [3], as a correction technique to normalize the observations to a standard angular configuration [4], as intrinsic surface signature used to retrieve bio-geophysical parameters [5], and as cross-calibration reference to radiometrically calibrate satellite sensors [6], [7]. However, there is currently a lack of extensive in situ validation data to assess the quality of BRDF data and modeling over different land covers. One of the major challenges in this respect is the spatial representativeness of the reference data and its comparability to the satellite pixel scale.

Many research activities focused on BRDF validation utilize ground-based multiangular instruments and satellite-based multiangular and multispectral data [2], [8], [9], [10], [11]. Although reflectances at any observation angle can be obtained using ground-based instruments, the measurement process is complex and time-consuming, affected by human interference, and only “punctual” measurements can be obtained. Moreover, the difficulties in accessing some areas and in assembling the in-site instrumentation lead to higher costs of the field campaign. Satellite remote sensing provides large area observations and multiangular imaging capability, even if several missions can work only from a few observation angles; on the other hand, spaceborne sensors have coarse spatial resolutions or poor revisiting times that hardly meet the needs of precise surface characterization [12].

The development of unmanned aerial system (UAS) technology offers the possibility of overcoming the above problems. In UAS-based applications, nadir observation data are mostly acquired [1], [13], while multiangular surveys are less used [15]. Recently, the use of the UAS for BRDF measurement and modeling of target surfaces is growing [16], [17], [18], [19], [20], but the measurement setup and data processing are often dissimilar, as well as the accuracy evaluation of the modeling is not always exhaustive.

The proposed work will analyze the reflectance angular distribution at two test sites. Reflectances will be measured by a UAS-based multispectral camera with multiangular acquisitions, and from a novel perspective with respect to the previous works, providing the following:

- 1) a theoretical discussion leading to a change on the common use of the “bidirectional” term in most experimental measurement contexts;
- 2) a dual “angular” approach in the data processing of the observed UAS imagery will be proposed as representative of measurements in the directional and conical configuration;
- 3) an evaluation of the BRDF modeling accuracy for both approaches.

The present methodology and outcomes are aimed at proposing an innovative multiangular UAS-based measurements collection protocol and their processing technique, looking forward to the systematic production of reference in situ validation datasets to improve and optimize the operational BRDF correction algorithms. A dual configuration approach (directional and conical) is tested and the corresponding “response” of the selected BRDF model is evaluated for one of the test sites (vegetation cover). This comparison is intended to provide a representation of the two different types of acquisition geometry that are most commonly considered when dealing with observations from space- and ground-based instruments, while it is not intended to be a fully comprehensive study of the entire angular domain that outlines a general rule. In particular, the dual configuration approach (directional and conical) for BRDF modeling by reflectances collected from UAS has not yet been explored in the literature to the best of our knowledge. A key aspect of the presented procedure is that the system and the used acquisition protocol allow for a very flexible data sampling, leading to a complete and optimal representativeness of the surface under investigation. A significant point is that the multispectral camera installed on the UAS and used in this study [21] is specifically designed to be compliant with the bands of the optical sensor installed onboard of Copernicus Sentinel-2 (S2) satellite [22]. This is a fundamental operational feature to support calibration/validation activities for satellite missions at higher spatial resolution, such as S2, where the knowledge of the reflectance angular distribution function for a surface plays a key role. A first qualitative comparison between S2 reflectances and Ross–Li–Maignan [23] derived reflectances over the Site 1 test area test area will also be outlined.

II. THEORETICAL BACKGROUND: TERMINOLOGY USAGE

Several literature articles refer to the BRDF derivation from satellite observations [3], [24] and, lately, from images acquired by UAS [18], [19], [25]. As pointed out in [1], the use of the “directional” term should be ascribed to infinitesimal solid angles which, in most experimental measurement contexts (from space–aerial–ground-based sensors), do not exist. Schaeppman-Strub et al. [1] consider as a “striking oversight” the assumption of the “measurements of the BRDF” since neither the incident irradiance nor the measured reflected radiation is properly

directional. Usually, incoming and reflected radiance observations are performed in a conical or hemispherical geometry, unless the instantaneous field of view (IFOV) of the sensor is adequately narrow to consider the radiance on it constant. In the text, we introduce the reflectance distribution (RD) acronym to indicate the angular distribution of the measured reflectances. We follow the practice to consider the angular characteristics of the incident radiance as named first, followed by the angular geometry of the reflected radiance, before the RD acronym.

A. Incident Radiation: Directional or Hemispherical?

For measured or derived Earth’s surface reflectances from satellite, aircraft/UAS or from the ground, the incident solar radiation geometry is hemispherical (H). Even if a solar zenith angle (SZA) is fixed, the incident radiation is not simply directional, as the BRDF term would seem to imply. The radiation reaching the surface, coming from the Sun’s direction, is the direct normal irradiance (or beam irradiance, W/m^2). But sunlight is also scattered back into space and toward the Earth’s surface, this term is called diffuse irradiance. Therefore, the total solar radiation incident on a horizontal surface (global irradiance) is the sum of the diffuse and the direct normal irradiance projected onto the horizontal surface. Under cloudless conditions, the diffuse irradiance is on the order of 15%–20% of the global hemispherical irradiance [26]. In fact, for reflectance measured by UAS with multispectral sensors, a hemispherical sunlight sensor is usually mounted on board to measure the global downwelling irradiance in each spectral band during the survey.

B. Reflected Radiation: Directional or Conical?

The most common observational configuration for spaceborne, airborne, and ground-based sensors is the hemispherical (H)–conical (C) one [1], leading to hemispherical conical-reflectance distribution (HC-RD) for multiangular acquisitions rather than bidirectional reflectance quantities.

From spaceborne optical sensors, the reflectance products are often derived by an integration over a narrow solid angle on the order of tenths of a degree, such as MODIS. In this case, the HC-RD can be considered as hemispherical directional-reflectance distribution (HD-RD), where HD stands for hemispherical (H)–directional (D).

Finally, some literature articles address the BRDF measurement and modeling by UAS [18], [19], neglecting the geometrical and angular specifications above. For instance, these works consider the overall surface reflectivity measured inside the sensor field of view (FOV) that can be on the order of 20° – 30° , providing an HC-RD rather than a bidirectional product.

Ultimately, the remote sensing measurement setup from different platforms does not properly provide bidirectional reflectance values and resulting RD functions should be considered as approximations of the BRDF.

III. MATERIALS

A. UAS Platform and Multispectral Sensors

The UAS used in this study consists of a high versatility hexarotor frame designed to support a take-off weight up to

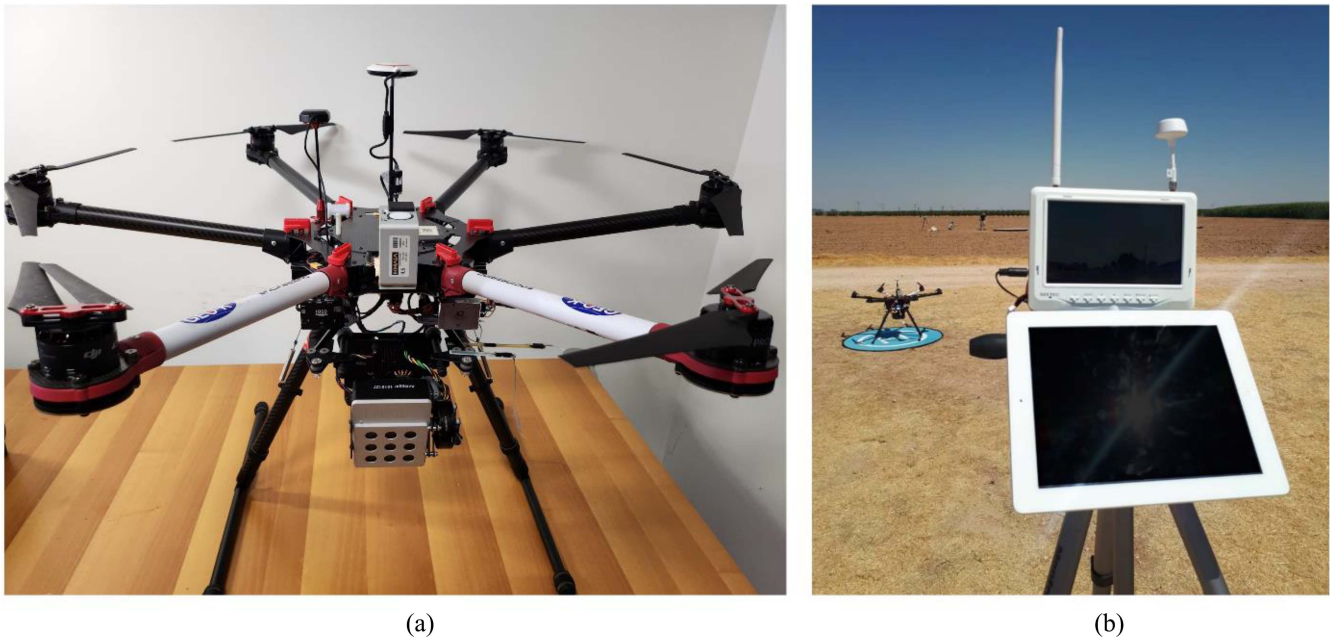


Fig. 1. (a) UAS with MAIA S2 multispectral camera on two-axis gimbal; ILS module with GPS antenna installed on top of the UAS. (b) Ground station.

TABLE I

SPECTRAL CHARACTERISTICS OF THE MAIA S2 MULTISPECTRAL CAMERA AND S2 MSI INSTRUMENT (SPECTRAL CHARACTERISTICS REFER TO PLATFORM SENTINEL-2A)

MAIA			S2		
Band	CWL (nm)	Band interval (nm)	Band	CWL (nm)	Bandwidth (nm)
B1	443	433–453	S1	442.7	20
B2	490	457.5–522.5	S2	492.7	65
B3	560	542.5–577.5	S3	559.8	35
B4	665	650–680	S4	664.6	30
B5	705	697.5–712.5	S5	704.1	14
B6	740	732.5–747.5	S6	740.5	14
B7	783	773–793	S7	782.8	19
B8	842	784.5–899.5	S8	832.8	105
B9	865	855–875	S8a	864.7	21

CWL=Central wavelength.

8.1 kg, with a maximum flight time up to 20 min and real-time mission management through a dedicated ground station (see Fig. 1). It is equipped with a DJI A2 flight unit, including inertial measurement unit and global positioning system (GPS) ensuring stabilized flight, and autonomous and repeatable surveys. The UAS has been designed and optimized for producing multiangular acquisition, using a programmable gimbal able to stabilize and tilt the multispectral camera according to the desired geometry. The main instrument on board is the MAIA S2 multispectral camera, providing high-resolution images at nine bands in the visible/near-infrared (VIS/NIR) electromagnetic spectrum regions (see Table I). MAIA S2 [21] has the same wavelength intervals as the European Space Agency (ESA) S2 multispectral instrument (MSI) sensor, as reported in Table I. The system is also equipped with an irradiance light sensor

(ILS), as shown in Fig. 1, measuring the hemispherical downwelling solar radiation in each MAIA band and allowing the correction for irradiance changes during the survey, such as those caused by clouds. The use of the ILS is crucial for the surface reflectance computation since it provides the reference values of the incident radiation for all bands at the exact time of shooting for each image. The MAIA S2 FOV is 35° horizontal and 26° vertical, with an image size of 1280 pixels \times 960 pixels. The IFOV related to every pixel is approximately 0.03° . When the flying height is 100 m, the ground spatial distance is 4.7 cm, and the image size is 60 m \times 46 m. The software used to process the raw file of MAIA S2 camera is provided by the producer. It is a professional software for geometric correction, coregistration, and radiometric correction of the multispectral images in the raw format. Radiometric correction also adopts a rigorous method

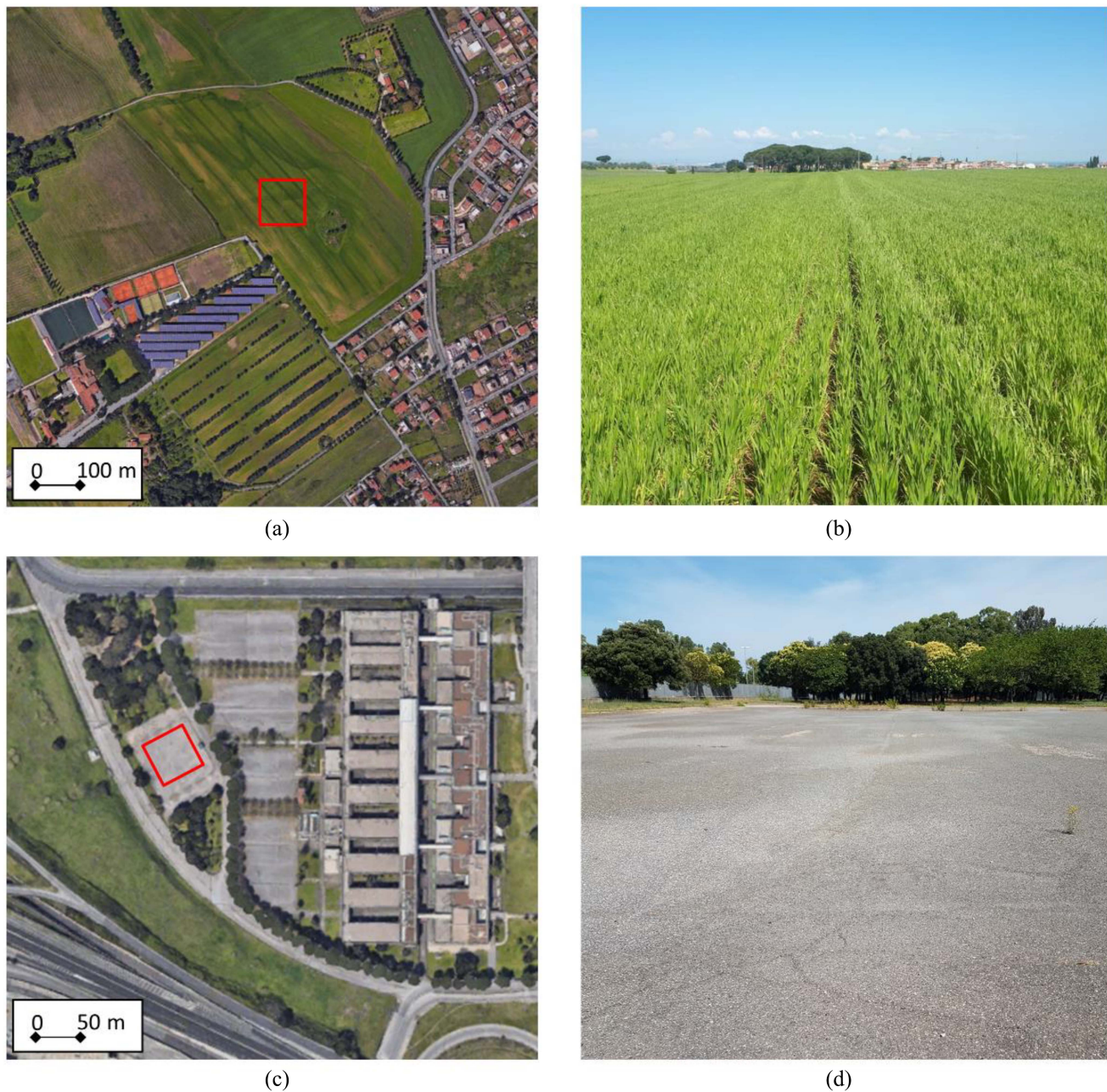


Fig. 2. Two test sites in Rome, Italy (source: Google Earth). (a) Site 1, vegetated area (latitude 41.876119°N, longitude 12.668271°E) and (b) on-ground picture collected in the moment of the survey. (c) Site 2, paved area (latitude 41.853472°N, longitude 12.601621°E) and (d) on-ground picture collected in the moment of the survey.

based on the ILS measurements to produce calibrated reflectance values at each band [21].

B. Study Area

Two test sites of different land covers were selected for the acquisition and processing of UAS MAIA S2 images (see Fig. 2). Each site was chosen with a coverage as homogeneous as possible. Besides, the capabilities of the system and the flexibility of the employed acquisition protocol allow for complete representativeness of the targeted surface even when changing viewing directions.

The first set of measurements was carried out on 30 April 2021 (around 12:45 local time, flight height 120 m) in a vegetated area, specifically a wheat field, close to the Borghesiana neighborhood in Rome, Italy, hereafter called “Site 1.” The SZA was 27° and the solar azimuth angle (SAA) was 169°.

The second set of measurements was acquired on 3 July 2021 (around 10:40 local time, flight height 10 m), considering a paved area, specifically an asphalt surface in the “Tor Vergata” University of Rome, hereafter called “Site 2.” The SZA was 37° and the SAA was 108°.

The survey time for both sites was about 15 min, during clear-sky conditions. A certain degree of uncertainty is related to the

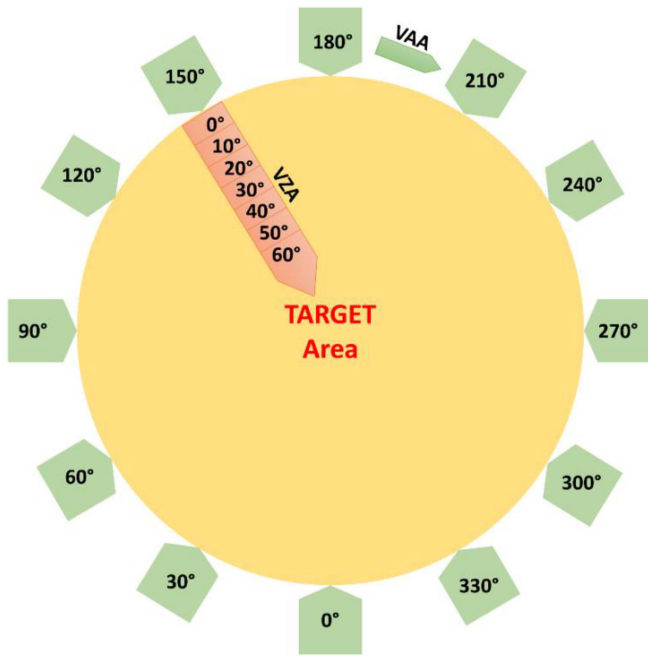


Fig. 3. Scheme of the flight planning for both sites: image acquisition at 12 VAA, from 0° to 330°, 30° step; for each VAA, 7 VZA, from 0° to 60°, 10° step, are considered.

change of SZA and SAA during the survey time: it is assumed that the Sun lies in a fixed position during the image acquisition (SZA and SAA values are selected at half of the survey).

IV. METHODOLOGY

A. RD Measurement Setup and Data Processing

We developed an ad hoc flight plan that mimics the goniometer acquisition systems, obtaining very high resolution multiangular dataset over a large scale and representative of the test sites, but overcoming the limitations of the on-ground installation of a goniometer, which are accessibility, installation costs, target representation, and integrity. The flight plan (see Fig. 3) shows a circular set of way points (green pins) in which the UAS stays in hovering for a few seconds and acquires pointing the camera toward the enclosed area looking at the center of the site with a specific camera tilt. The obtained dataset consists of MAIA S2 multispectral acquisitions collected for 7 different view zenith angles (VZAs), by controlling the angle of the gimbal, and 12 different view azimuth angles (VAAs), for a total of 84 images for each band. Specifically, the VAA ranges from 0° to 330° with a step of 30°, and the VZA from 0° to 60° with a step of 10°. The UAS covers all the VAAs for a fixed VZA, i.e., for the VZA of 0°, the VAAs are covered from 0° to 330°, then the inclination of the camera is increased by 10° and all VAAs are scanned, and so on. The flight plan is stored in the ground station and automatically executed by the UAS, ensuring the best accuracy and repeatability over time and different target surfaces.

Since the MAIA vertical FOV is 26° in the VZA direction, the multiangular observation data with a 10° step cause a theoretical overlapping of 16° between two consecutive image acquisitions: this data overlapping has to be eliminated in one of the two

images. In the azimuth direction, with a horizontal FOV of 35°, the theoretical overlapping of two consecutive VAA (30° step) is only 5°.

The data processing for the RD computation followed two approaches.

- 1) *HC-RD (conical configuration)*: A cone angle of 10° vertical and horizontal (subtending about 370 × 370 pixels) is considered for each specific acquisition geometry (specifically, ± 5° steps around the VZA), discarding the areas of the image, which do not frame the target surface. This cone angle avoids data overlapping between two consecutive images. A single value of reflectance is computed by averaging the reflectances of the pixels of the subtended area, for a total of 84 measurements for each band.
- 2) *HD-RD (directional configuration)*: A cone angle of 3° vertical and horizontal (subtending about 110 × 110 pixels) is considered for each specific acquisition geometry, discarding the areas of the image, which do not frame the target surface. A single value of reflectance is computed by averaging the reflectances of the pixels of the subtended area, for a total of 252 measurements for each band. Assuming a uniform RD over the selected angle, the signal can be considered as acquired in a directional configuration. A configuration with angles lower than 3° was not considered because the subtended area, consisting of a few pixels, would not always have guaranteed representativeness of the land cover under investigation.

Reflectance patterns will be represented in a polar coordinate system to better interpret and compare the data in the zenith-azimuth angular domain at the different spectral bands.

B. BRDF Model

The multiangular measurements made by the UAS at the two sites, with both approaches, can be used to infer a BRDF model for any viewing zenith/azimuth angles in the different spectral bands. The model was derived by taking the UAS reflectance measurements as input observations and fitting a modified version of the kernel-driven RossThick–LiSparse (Ross–Li) semiempirical linear model, called Ross–Li–Maignan [23]. Since in the Ross–Li model, operationally used for the MODIS BRDF products [3], [24], [27], the volumetric kernel does not consider the hotspot effect (which accounts for the reflectance increase that takes place when the Sun and the view directions are coincident), the Ross–Li–Maignan model was adopted to bridge this gap. Although other modified versions of the standard Ross–Li model were implemented [28], the Ross–Li–Maignan formulation has proved to fit with high accuracy the hotspot signature and it has shown to have good performance also in comparison with other BRDF models [23].

Given a specific surface, this model can be used to simulate the reflectance anisotropy at any viewing and illumination geometry. The Ross–Li model is a linear combination of basic scattering kernels expressed as follows:

$$R(\theta_s, \theta_v, \varphi; \lambda) = f_{\text{iso}} + f_{\text{vol}} K_{\text{vol}}(\theta_s, \theta_v, \varphi; \lambda) + f_{\text{geo}} K_{\text{geo}}(\theta_s, \theta_v, \varphi; \lambda) \quad (1)$$

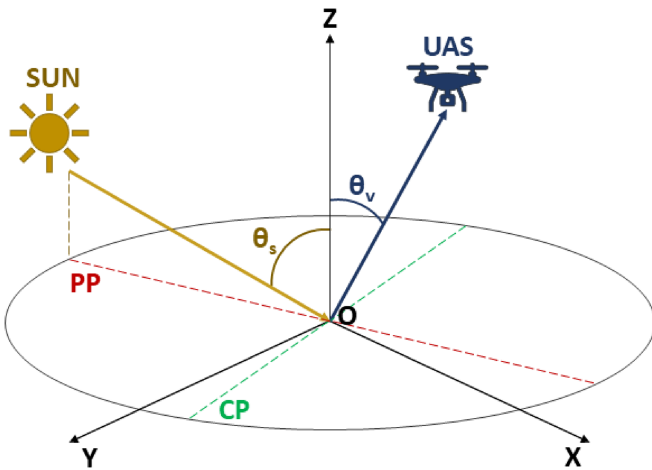


Fig. 4. Scheme of the viewing and illumination geometry in a generic UAS-sun configuration. Definition of principal plane (PP, dashed red line), cross plane (CP, dashed green line), sun zenith angle θ_s (SZA), and VZA θ_v .

where R is the reflectivity at wavelength λ , θ_s is the SZA, θ_v is the VZA, ϕ is the view-Sun relative azimuth angle ($\phi_v - \phi_s$); K_{geo} is the geometric optical kernel (LiSparse kernel) derived by Li and Strahler [29]; K_{vol} is the volumetric scattering kernel (RossThick kernel) initially derived by Roujean et al. [30], and successively modified by Maignan et al. [23] in order to take into account the hotspot effect. These kernels describe the fundamental physical theory of the volumetric and surface scattering. The coefficients f_{iso} , f_{vol} , and f_{geo} represent the proportion of the isotropic reflection, volumetric, and geometric scattering, respectively. These three model parameters can be obtained by fitting the multiple observed reflectances (multiangular and multispectral) using a least square approach, after calculating K_{vol} and K_{geo} for each measurement point with its specific acquisition geometry.

It is important to point out that (1) provides a BRDF modeling since θ_s , θ_v , and ϕ can be supplied as specific directions in the reflectance simulations. As reported in Section II, remote sensing observations used to fit the model do not properly provide bidirectional reflectances (a hemispherical diffuse irradiance is summed to the beam irradiance at θ_s , and the IFOV may not be narrow enough), leading to an approximated measurement of the BRDF.

In this work, the input reflectance measurements refer to the SZA and SAA of the two experimental campaigns, reported in Section III-B. In Section VI, the modeling issues will be reported.

V. RESULTS

A. HC-RD/HD-RD Measured Patterns (Site 1)

In this section, the results of the HC-RD and HD-RD measurements by MAIA S2 at the different spectral bands will be reported for Site 1. In general, by using a polar coordinate system to represent the zenith-azimuth angular patterns, the solar principal plane (PP) and the cross plane (CP) can be highlighted (see Fig. 4). The solar PP is the vertical plane containing both the incident ray of the Sun and the zenith direction (dashed red line in Fig. 4); the CP is orthogonal to the PP (dashed

green line in Fig. 4). The two planes identify the backward (the CP side with the Sun) and the forward direction (the CP side opposite with respect to the Sun) of the scattered radiation. For example, surfaces with a certain degree of roughness, such as vegetated area, are expected to exhibit a reflectance prevalence in the backward direction, while flat surfaces in the forward direction (specular scattering). In Fig. 4, the VZA θ_v , i.e., the angle between the local zenith and the UAS line of sight from the sensor to the surface, and the Sun zenith angle θ_s (SZA), i.e., the angle between the local zenith and Sun line of sight from the Sun to the surface, are also displayed.

In the following polar plots representing reflectances measured by MAIA camera (see Figs. 5, 7, and 10), the cross points between the radius (i.e., VAAs) and the concentric circles (i.e., VZAs) correspond to the reflectance value measured by MAIA camera, while the areas in between refer to the interpolated value of reflectance. Note that the polar diagrams describe a different configuration geometry compared with the flight plan in Fig. 3, which is intended to depict instead how and where the acquisitions are collected by the UAS.

1) *Approach 1: HC-RD (10° FOV)*: The HC-RD polar plots for the measurements collected 30 April 2021 on Site 1 considering a cone angle of 10° are shown for all bands of the MAIA multispectral camera (see Fig. 5).

Given the wide variability of the reflectance values in the different bands for vegetated surfaces, different color scales have been used for a better visualization of the reflectance angular dynamic. For VIS bands, the main variations of the HC-RD are observed close to the PP, i.e., in the plane where the Sun lies, with the higher values in correspondence of the Sun position, i.e., in the backward direction, as expected from a vegetated area. When the sensor is facing away from the Sun (backscattering direction), it sees the well-illuminated side of the vegetation, which gives higher reflectance; when the sensor is facing the Sun (forward scattering direction), it sees instead the shadowed side of the vegetation, which leads to lower reflectance. In the RedEdge (RE) NIR bands, the anisotropic effects are less evident in the viewing azimuth directions, while it grows by increasing VZA. This is because the shadows are weaker due to a smaller absorption of radiance by chlorophyll in the NIR spectral range [31].

The spectral signature at different VZAs (from 0° to 60° for a VAA of 180° (close to the PP) is reported in Fig. 6.

The VAA of 180° corresponds to the direction close to the Sun azimuth position (PP) in the backward scattering direction. The reflectance curves describe a typical vegetation target in the VIS-NIR spectrum, and the increase of VZA leads to an overall increase of the reflectance values in each band except for the bands that exhibit a more pronounced hotspot effect, such as B4, for which a local increase of reflectance in the VZAs close to the SZA is observed (see the lower value of reflectance of the curves at VZA 50° and 60° compared with the curve at 20° and 30°, which indeed are closer to the SZA).

2) *Approach 2: HD-RD (3° FOV)*: The HD-RD polar plots for the measurements collected 30 April 2021 on Site 1 considering a cone angle of 3° are shown for all bands of the MAIA multispectral camera (see Fig. 7).

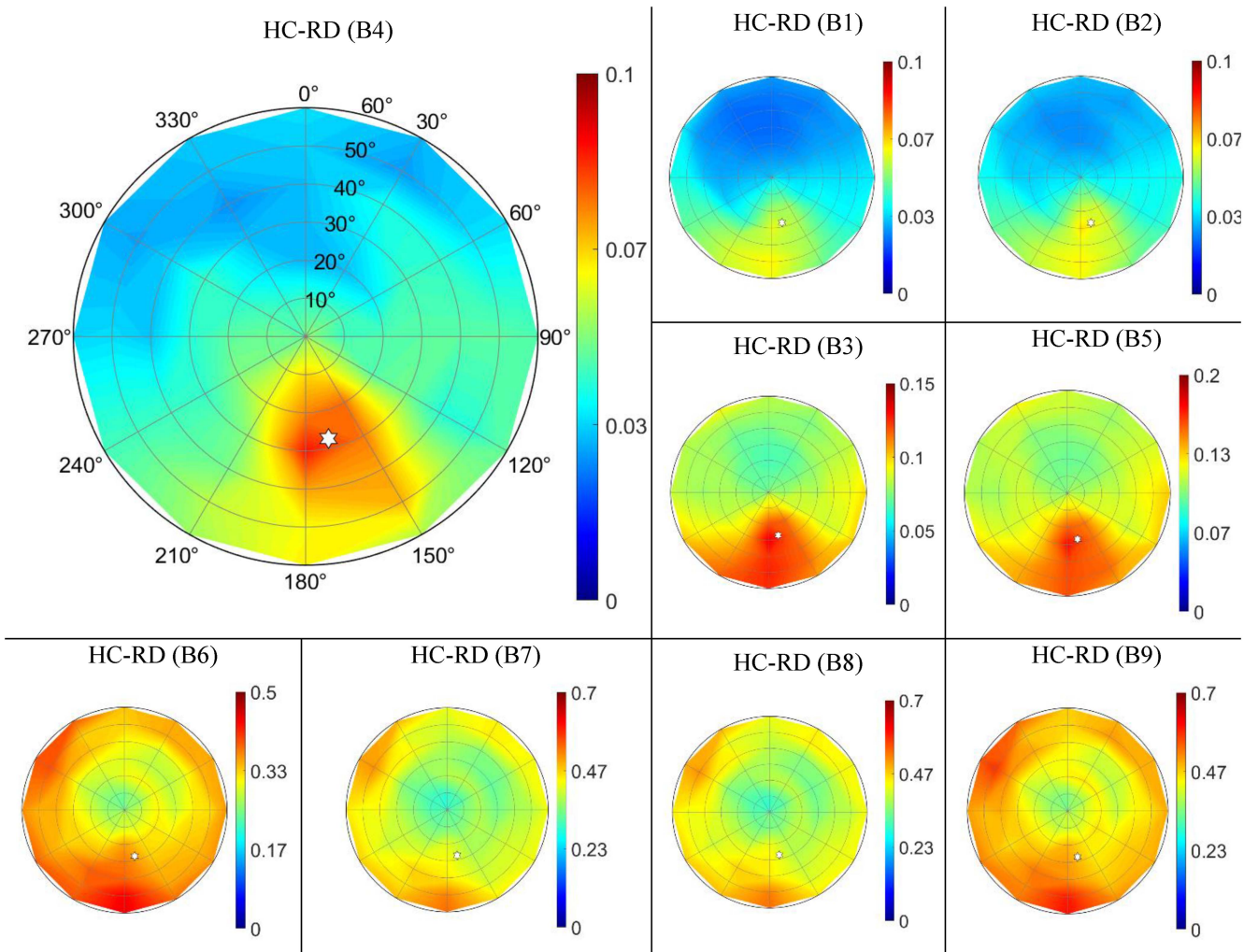


Fig. 5. HC-RD polar plots for the nine bands of MAIA multispectral camera for site 1 considering a cone angle of 10° . The white star indicates the Sun position at the time of the field campaign. Be aware of the color scaled on the side of the polar diagrams for understanding of the reflectance dynamic.

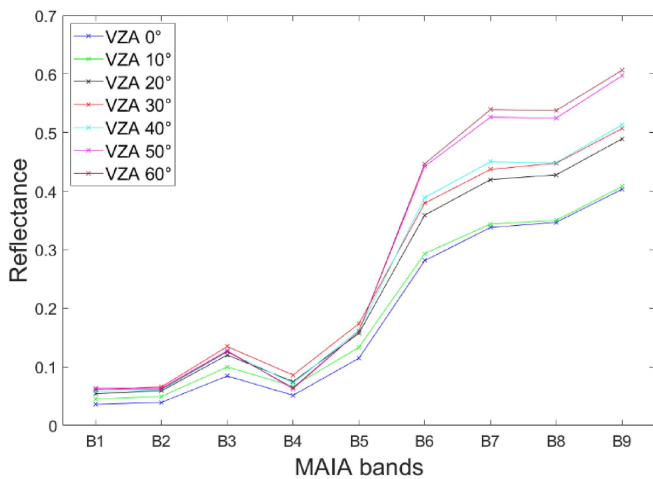


Fig. 6. Site 1, 10° FOV: spectral signature observed by MAIA at different VZAs (from 0° to 60° with a step of 10°) for a VAA of 180° (close to the PP). The SZA is 27° and the SAA of 169° .

The same general considerations of Fig. 5 are valid for Fig. 7; the dynamic of the reflectance along the VZA, VAA, and bands is the same for the two approaches. However, we want to specify that, in this case (cone angle of 3°), the grid in the polar diagram is denser, given the procedure adopted to retrieve the reflectance dynamic (see Section IV-A), which involves a total of 252 measurements for each band. More complex and structured behavior of the HD-RD can be observed compared with the HC-RD. The latter has indeed a smoother pattern than the former, given the lower number of observations each of which is averaged over a wider area for HC-RD (about 370×370 pixels) compared with HD-RD (about 110×110 pixels).

3) *Comparison Between Approaches 1 and 2:* In Table II, the root-mean-square difference (RMSD), the relative RMSD (rRMSD, i.e., the ratio between RMSD and the mean on the observed dataset that facilitates the comparison between datasets with different scales), and the correlation coefficient (CC) between reflectances measured for both HC-RD and HD-RD approaches are reported for each MAIA band for Site 1. For each band, the comparison is performed over

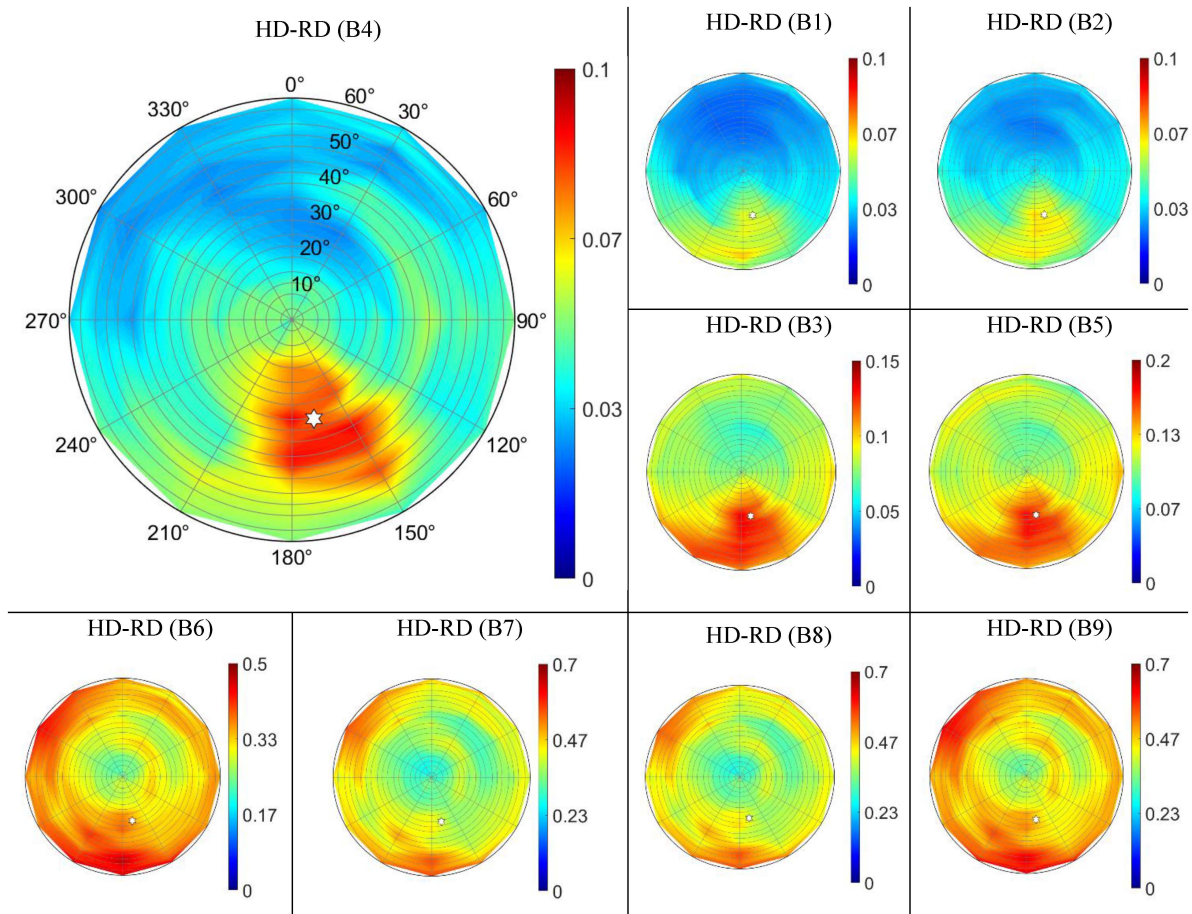


Fig. 7. HD-RD polar plots for the nine bands of MAIA multispectral camera for site 1 considering a cone angle of 3° . The white star indicates the Sun position at the time of the field campaign. Be aware of the color scaled on the side of the polar diagrams for understanding of the reflectance dynamic.

TABLE II
RMSD, rRMSD, AND CC FOR EACH BAND BETWEEN REFLECTANCES
ACQUIRED BY HC-RD AND HD-RD APPROACHES FOR SITE 1

Band/central wavelength	RMSD	rRMSD	CC
B1 - 443 nm	0.0015	0.0426	0.99
B2 - 490 nm	0.0019	0.0477	0.98
B3 - 560 nm	0.0033	0.0383	0.98
B4 - 665 nm	0.004	0.0865	0.96
B5 - 705 nm	0.0051	0.0432	0.96
B6 - 740 nm	0.0158	0.049	0.97
B7 - 783 nm	0.0219	0.0564	0.96
B8 - 842 nm	0.0218	0.0557	0.96
B9 - 865 nm	0.0236	0.0526	0.96

the 84 HC-RD measurement samples by selecting the corresponding HD-RD measurements at the same geometrical pointing.

The low values of RMSD and rRMSD in Table II lead us to infer that the HC-RD and HD-RD approaches are in good agreement with each other, i.e., the difference in the reflectance values between them is small. This is also confirmed by the high value of the CC. A general increase of the RMSD between the two procedures can be observed moving from VIS bands to RE-NIR bands since the reflectance dynamic range increases,

while the rRMSD is quite uniform across the bands, except for band 4.

B. Modeling of HC-RD/HD-RD Measurements (Site 1)

With reference to Section IV-B, once MAIA data have been processed and reflectance values have been extracted for each VZA and VAA, at fixed SZA and SAA, the dataset is used to find the parameters f_{iso} , f_{vol} , and f_{geo} of the semiempirical Ross–Li–Maignan model (1), which best fit the measurements (after computing K_{vol} and K_{geo} by knowing the Sun and acquisition geometries). The MATLAB curve fitting toolbox, based on the least squared method, was used to fit the reflectance observations. Retrieved model parameters can then be used in forward model runs to reproduce reflectances for any viewing geometry.

In this section, a comparison between the measured and the modeled patterns, obtained by running the forward model for the same acquisition geometry of the measured data, is reported for Site 1.

Fig. 8 reports the fitted model parameters f_{iso} , f_{vol} , and f_{geo} for each band of the MAIA multispectral camera considering the multiangular reflectances obtained by both approaches 1 and 2, i.e., HC-RD and HD-RD measurements.

TABLE III
RMSE, rRMSE, AND CC BETWEEN MEASUREMENTS AND MODELED REFLECTANCES FOR EACH BAND AND FOR HC-RD AND HD-RD APPROACHES (SITE 1)

Band/central wavelength	HC-RD			HD-RD		
	RMSE	rRMSE	CC	RMSE	rRMSE	CC
B1 - 443 nm	0.0036	0.0979	0.94	0.0039	0.109	0.93
B2 - 490 nm	0.0032	0.0821	0.94	0.0039	0.099	0.92
B3 - 560 nm	0.006	0.0684	0.92	0.0071	0.0817	0.9
B4 - 665 nm	0.0049	0.1049	0.92	0.0071	0.1531	0.86
B5 - 705 nm	0.0078	0.0653	0.9	0.0097	0.0816	0.85
B6 - 740 nm	0.026	0.0813	0.84	0.0302	0.095	0.81
B7 - 783 nm	0.0346	0.0895	0.81	0.0413	0.1079	0.78
B8 - 842 nm	0.0341	0.0875	0.8	0.041	0.1059	0.77
B9 - 865 nm	0.0372	0.0832	0.79	0.0441	0.0993	0.76

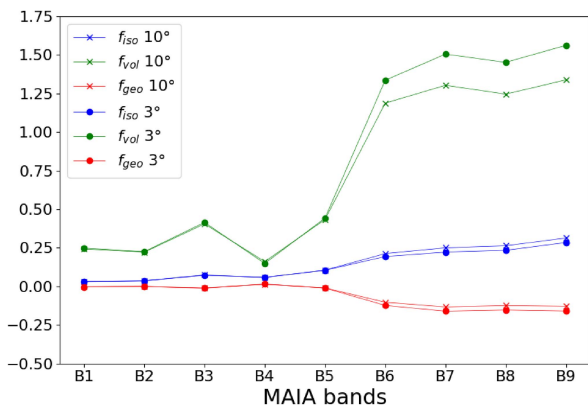


Fig. 8. Site 1: parameters f_{iso} , f_{vol} , and f_{geo} of the Ross–Li–Maignan model for each band of MAIA and for both HC-RD (10° FOV) and HD-RD (3° FOV) approaches.

As previously highlighted, f_{iso} , f_{vol} , and f_{geo} represent the proportion of the isotropic reflection, volumetric, and geometric scattering, respectively. For this vegetated surface, the f_{vol} parameter is predominant among others, especially above $B6$ (750 nm): this seems reasonable being the vegetation surface mostly dominated by a volumetric scattering mechanism. Furthermore, f_{iso} has a greater weight with respect to f_{geo} and it grows above $B5$ (700 nm).

In Table III, the root-mean-square error (RMSE), the relative RMSE (rRMSE), and the CC between measured and modeled reflectances are reported for both HC-RD and HD-RD approaches for Site 1. These metrics give a quantitative insight of the model’s accuracy in representing the observed reflectances.

Fig. 9 displays the modeled HC-RD (right column) and HD-RD (left column) for $B3$ and $B8$ MAIA bands of Site 1.

According to the metrics in Table III, the performance of the model is higher using the approach which considers measurements with a cone angle of 10° to feed the Ross–Li–Maignan model. Indeed, both the RMSE and the rRMSE are smaller and the CC is higher for the HC-RD approach compared with the HD-RD metrics. In particular, the maximum rRMSE is of 10% for the HC-RD approach, while the maximum rRMSE is of 15% for the HD-RD approach. In other words, for the methodology adopted in this work and given the Ross–Li–Maignan model,

measurements that involve a more homogeneous and wider survey area (370×370 pixels for a cone angle of 10°) can be better replicated by the specific model under consideration. Looking at Fig. 9 is pretty straightforward to notice that both model simulations for the HC-RD and HD-RD approaches exhibit a smoothed dynamic of the reflectance, despite the latter being derived by a denser grid and a higher number of observations. This leads us to consider that the Ross–Li–Maignan model is not able to entirely capture and replicate articulated and detailed reflectance behavior even if fed with a larger number of observations. Thus, the Ross–Li–Maignan model exhibits best fitting performances when considering the measurement protocol with a cone angle of 10° instead of a cone angle of 3° for the retrieval of the reflectance values according to the analysis presented in this study. The rRMSE computed solely along the PP for Site 1 is less than 10% for the HC-RD configuration, proving a similar fitting ability of the Ross–Li–Maignan model for both the PP and the entire set of data, as analyzed in Table III. It has to be noticed that the data selected to compute the rRMSE along the PP are the closest ones from the Sun’s geometry.

C. Measurements and Modeling for Site 2

In this section, the results obtained for the HC-RD measurements by MAIA S2 at the different spectral bands will be reported for Site 2.

Following the analysis made for HC-RD and HD-RD for Site 1, where an overall better performance of the forward Ross–Li–Maignan model in replicating HC-RD values for the procedure developed in this work was found, the description of the results for the asphalt field campaign (Site 2) is, therefore, outlined considering the reflectances collected in a cone angle of 10° (370×370 pixels).

However, the comparison between the measurements in the HC-RD and HD-RD configuration has been carried out also for Site 2 and it is summarized in Table IV for the sake of brevity, where the RMSD, rRMSD, and CC for each MAIA band are reported.

From the metrics in Table IV, a low level of discrepancy is observed between the two approaches. Comparing the results of Tables II and IV, a smaller difference between HC-RD and HD-RD approaches for Site 2 is found with respect to Site 1.

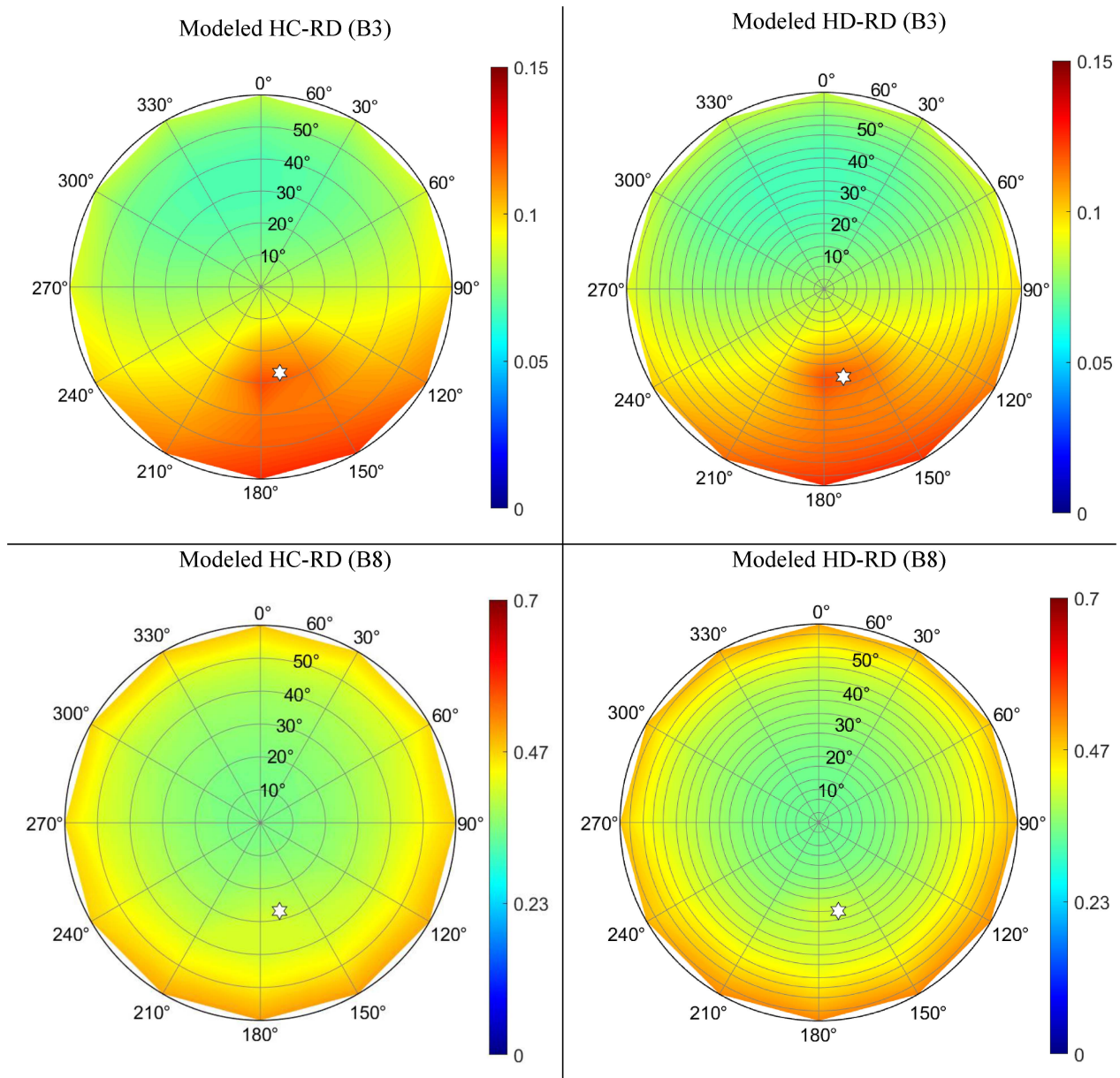


Fig. 9. Site 1: polar plots of the simulation by Ross–Li–Maignan model of the HC-RD and HD-RD measurements for the B3 and B8 MAIA bands.

The rRMSD is indeed around the 2% for Site 2 compared with 5% for Site 1.

The HC-RD polar plots for the measurements collected on 3 July 2021 on Site 2 considering a cone angle of 10° are shown for all bands of the MAIA multispectral camera (see Fig. 10).

From Fig. 10, a prevalent backward scattering mechanism can be observed for the asphalt site. The same backward scattering was observed also for the vegetation site (see Fig. 5) with the difference that the reflectance peak is more pronounced for vegetation, while for asphalt, the maximum of the reflectance is more spread in all the backward plane of the polar diagram. This behavior can be explained considering the presence of medium–high elements for the vegetation area, which are not present instead in the asphalt area that is characterized by a relatively homogeneous degree of roughness. Moreover, the roughness of

the asphalt site is also the reason why the polar diagrams do not exhibit a forward scattering mechanism (specular reflection), as would be expected for a perfectly flat surface. Besides, a narrower range of variability of the reflectance values among MAIA bands can be observed for Site 2 compared with Site 1.

The spectral signature at different VZAs (from 0° to 60°) for a VAA of 120° (close to the PP) is reported in Fig. 11.

The reflectance in Fig. 11 shows a trend in accordance with the hotspot effect. The spectral signatures highlight indeed a maximum of the reflectance lying between the VZA 20° and 50° curves, as expected since the SZA is around 37° at the time of the field campaign and given that the surface is characterized by a backward scattering mechanism. The red and the cyan curves (VZA 30° and 40° , respectively), i.e., the curves with VZA closer to the SZA, exhibit indeed the highest reflectance values. A

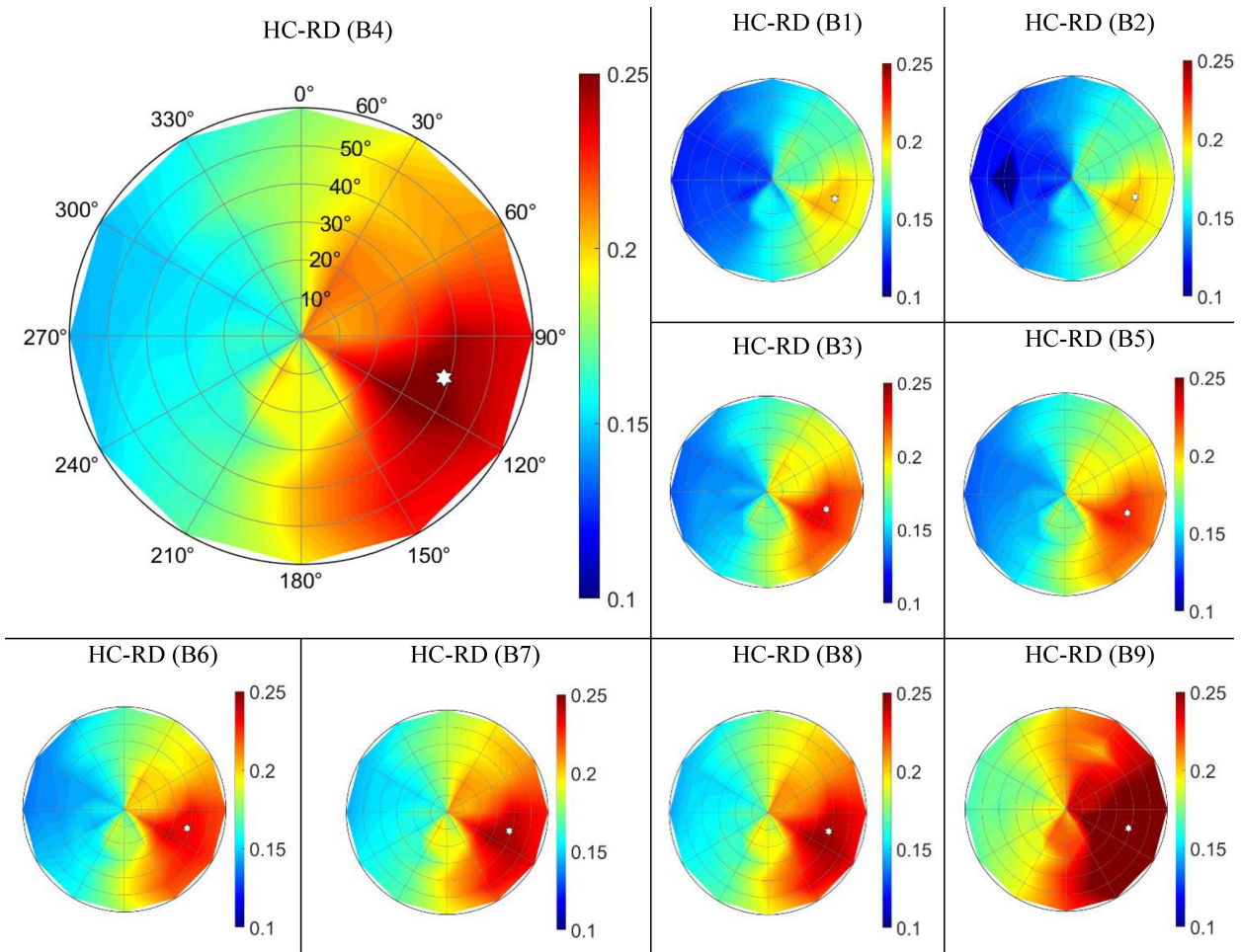


Fig. 10. HC-RD polar plots for the nine bands of MAIA multispectral camera for Site 2 considering a cone angle of 10° . The white star indicates the Sun position at the time of the field campaign.

TABLE IV
RMSD, rRMSD, AND CC BETWEEN REFLECTANCES ACQUIRED BY HC-RD AND HD-RD APPROACHES FOR SITE 2

Band/central wavelength	RMSD	rRMSD	CC
B1 - 443 nm	0.0035	0.0226	0.99
B2 - 490 nm	0.0032	0.0213	0.99
B3 - 560 nm	0.0039	0.0227	0.99
B4 - 665 nm	0.0044	0.0233	0.99
B5 - 705 nm	0.004	0.0232	0.99
B6 - 740 nm	0.0044	0.0244	0.99
B7 - 783 nm	0.0043	0.0228	0.99
B8 - 842 nm	0.0043	0.0225	0.99
B9 - 865 nm	0.0049	0.0228	0.99

narrower range of the reflectance dynamic along the bands (from about 0.16 to about 0.28) can be observed compared with the range for the vegetation site (from about 0.04 to about 0.6, see Fig. 6) characterized by a greater reflectance variability.

As can be noted from the polar plots for Site 1 and Site 2, the anisotropic effects depend on several factors: the type of surface under examination, the hotspot effect in correspondence to the Sun position, the VZA, the VAA, and the spectral bands.

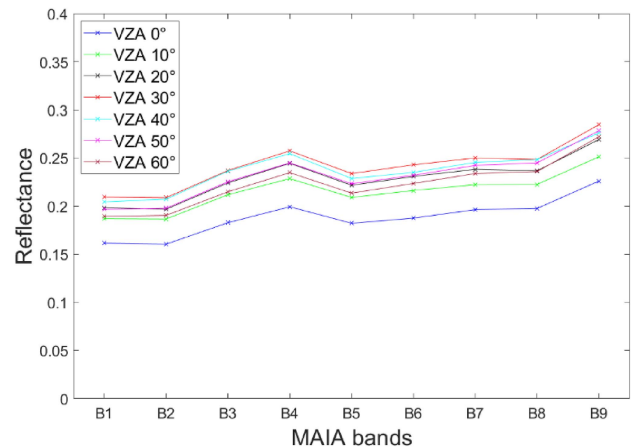


Fig. 11. Site 2, 10° FOV: spectral signature observed by MAIA at different VZAs (from 0° to 60° with step of 10°) for a VAA of 120° (close to the PP). The SZA is 37° and the SAA 108° .

Fig. 12 reports the fitted model parameters f_{iso} , f_{vol} , and f_{geo} for each band of the MAIA multispectral camera considering the multiangular reflectances obtained by the HC-RD approach for Site 2.

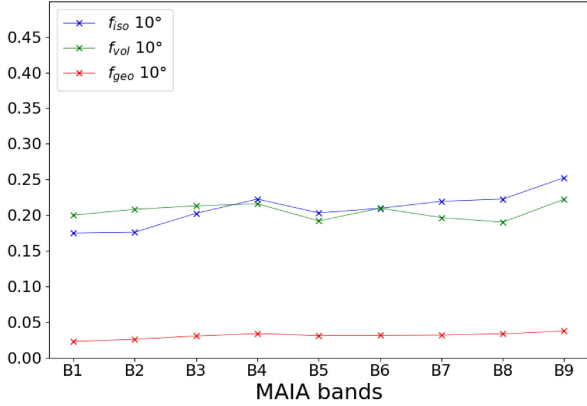


Fig. 12. Site 2: parameters f_{iso} , f_{vol} , and f_{geo} of the Ross–Li–Maignan model for each band of MAIA and for HC-RD (10° FOV) approach.

TABLE V

RMSE, rRMSE, AND CC BETWEEN MEASUREMENTS AND MODELED REFLECTANCES FOR EACH BAND FOR THE HC-RD APPROACH (SITE 2)

Band/central wavelength	RMSE	rRMSE	CC
B1 - 443 nm	0.0116	0.0755	0.87
B2 - 490 nm	0.0135	0.0884	0.86
B3 - 560 nm	0.0131	0.0755	0.88
B4 - 665 nm	0.0135	0.0708	0.89
B5 - 705 nm	0.0123	0.0707	0.89
B6 - 740 nm	0.0125	0.0695	0.89
B7 - 783 nm	0.0115	0.0608	0.9
B8 - 842 nm	0.0107	0.0565	0.92
B9 - 865 nm	0.0121	0.0559	0.92

Fig. 12 shows that, for the asphalt surface, the f_{iso} parameter is predominant among others from $B4$ onward, while the f_{vol} parameter is predominant from $B1$ to $B3$. f_{geo} is the parameter showing less contribution. In general, the Ross–Li–Maignan parameters retrieved for the asphalt surface are less spectrally variable than the parameters retrieved for the vegetated surface.

Table V reports the RMSE, the rRMSE, and CC between measurements and modeled reflectances for the HC-RD approach for Site 2.

The metrics in Table V highlight that the reflectances simulated with the Ross–Li–Maignan model are in good agreement with the reflectances measured in the asphalt field campaign. The maximum rRMSE is indeed less than 9%. The rRMSE values are slightly better than the ones found for the HC-RD in Table III for the vegetation field campaign, and an increase in the model accuracy is observed going to VIS to NIR for Site 2. The rRMSE computed solely along the PP for the Site 2 is less than 9% for the HC-RD configuration. This result proves again the same fitting ability of the Ross–Li–Maignan model for both the PP and the entire dataset, as reported in Table V. As for the computation of rRMSE along the PP for Site 1, the data used to compute the rRMSE along the PP are the closest ones from the Sun’s geometry also for Site 2.

Overall, the Ross–Li–Maignan model exhibits good performances when applied to HC-DR measurements for both sites, with a rRMSE below 10%.

VI. DISCUSSION

The UAS technology with multiangular imaging capability proved its potential for reflectance pattern measurement and BRDF modeling of target surfaces. However, the measurement setups and data processing are often dissimilar and not standardized, as well as the accuracy evaluation of the modeling. In this work, we proposed a UAS-based experimental campaign at two test sites analyzing a dual “angular” approach (HC-RD and HD-RD) in the data processing as representative of measurements in the directional and conical configurations, usually considered when dealing with observations from space- and ground-based instruments. The comparison between the two approaches in terms of measured reflectance patterns and the corresponding metrics shows a high agreement between the two operating modes; however, a more variable pattern of the HD-RD was observed with respect to the HC-RD. The HC-RD has a smoother pattern as expected due to the lower number of observations and the averaging over a wider area.

Concerning the modeling of the measurements between the two approaches in relation to Site 1, both model simulations exhibit a similar smoothed reflectance dynamic, despite HD-RD being derived by a denser angular grid and a higher number of observations. With regard to the procedure developed in this work, it can be observed that the Ross–Li–Maignan model shows the best fitting performance when considering the UAS measurement protocol with a cone angle of 10° instead of 3° . In future works, we aim to obtain higher accuracy of modeled reflectances through the development of an advanced model based on neural networks (NNs). If in fact the development of more detailed BRDF kernel-based models involves the design of ever more complicated formulation of the kernels describing the scattering mechanisms, the NN-based algorithms are an effective tool for solving nonlinear complex problems, which involve the interdependence of many variables. Moreover, the UAS technology has proved to be a very efficient instrument to quickly and easily collect extensive multiangular reflectance measurements that can be used as a robust and representative dataset for the training of a NN model. The possibility to set up a NN model for the retrieval of reflectances at different viewing and illumination geometries with higher performances compared with the standard BRDF models would be a significant step forward toward the development of ever more refined and accurate BRDF correction techniques for satellite sensors.

As reported previously, the MAIA S2 multispectral camera used in this study has the same bands as the S2 satellite. This is a fundamental operational feature to improve calibration/validation activities for satellite missions at higher spatial resolution, such as S2.

A. Comparison Between Copernicus S2 Measurements and Modeled Reflectances

By way of preliminary investigation and without presuming to provide a full and exhaustive assessment, a qualitative comparison between reflectance measured by S2 sensor and reflectance generated from the Ross–Li–Maignan model at the same viewing and illumination geometry of S2 sensor is reported

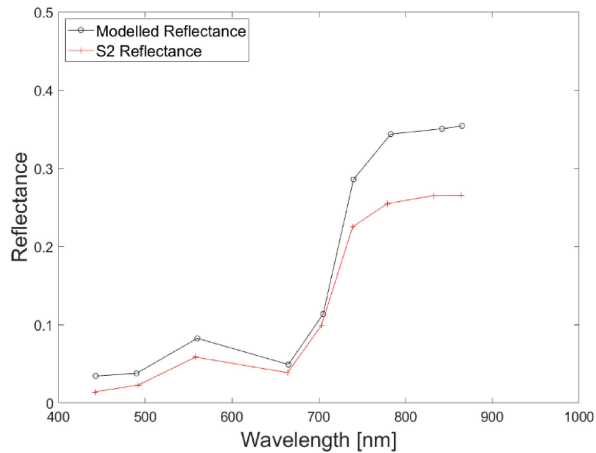


Fig. 13. Reflectance patterns for S2 MSIL2A product collected on site 1 area 30 April 2020 at 10:00 UTC [T33TUG] with VZA 2.5°, VAA 111°, SZA 29.7°, and SAA 151° (red curve) and Ross–Li–Maignan simulations generated at the same viewing and illumination geometries of S2 (black curve).

in Fig. 13. The S2 MSI Level-2A product providing atmospherically corrected surface reflectance [32] has been used.

Net of possible atmospheric interference due to adjacent clouds and particular aerosol effects, the comparison between the S2 reflectance on Site 1 and the Ross–Li–Maignan reproduced reflectance shows how the pattern is similar, albeit a wider gap between the S2 and the modeled reflectance is recorded for the NIR bands, i.e., the most spectrally sensitive to vegetation, compared with the VIS/RE bands. The latter aspect may be related to a more accurate target representation obtained using the UAS platforms, which acquire at centimeter spatial resolution and low altitudes drastically reducing both spectral mixing problems and atmospheric interferences inherent to satellite platforms. The different spatial representativeness of UAS and S2 MSI sensor introduces a certain degree of uncertainty in the comparison, despite the S2 data in Fig. 13 have been preprocessed to obtain a 10-m spatial resolution for all the S2 bands (which is quite high for satellite optical sensors). According to the developed flight strategy, the UAS-based dataset shows high performance in surface characterization, which leads to more accurate Ross–Li–Maignan model parameters retrieval. The idea behind this qualitative comparison is to provide an example of possible operational use of UAS-based BRDF computation, as the proposed UAS and acquisition protocol proves to be valuable support for validation and calibration activities of the S2 sensor reflectance. A more comprehensive and detailed analysis of the discrepancies between S2 and modeled reflectances requires a focused study involving a comparison with a large and diverse amount of S2 data, which is beyond the scope of the present work.

In the following, further issues of the BRDF modeling procedure, UAS potential and uncertainty, and future research directions are highlighted.

B. Modeling Issues

- 1) The chosen kernel-driven Ross–Li–Maignan semiempirical linear model gives reasonable fits to field-measured

reflectance datasets, and it is able to accurately represent the angular reflectivity patterns of different surfaces [33]. Since the model is linear and has few parameters, it can be more easily and quickly inverted, albeit models with more parameters may be generally highly accurate [30]. Besides, it is preferable when the input dataset has a sparse angular sampling: a limit of this work is the model implementation with input reflectance measurements referred to the SZA and SAA of the two experimental campaigns.

- 2) The performance of a model is driven by the accuracy of the estimated parameters; therefore, the quality of the observed reflectances is fundamental. The field data should be acquired under sufficient angular sampling, under clear-sky condition and in a brief time interval so that the surface’s characteristics and the atmospheric conditions do not change during the acquisition period. Moreover, the performance of a model to simulate the reflectance directional signature depends on the land covers [34].
- 3) The existing kernels of the kernel-driven models are based on a physical approximation of a hypothetical scenario. Therefore, kernels have different adaptabilities for different scenarios: if the application scenario deviates significantly from the kernel assumptions, the kernel-driven model can exhibit poor performance.
- 4) The Ross–Li–Maignan model performs well under most observational conditions. As found by Li et al. [34], under different Sun-sensor geometries, the fitting ability is positively correlated with SZA, showing poorer accuracy when SZA is large.

C. UAS Potential and Uncertainty

- 1) UAS market is experiencing a rapid development, then the exploitation of UAS potential requires knowledge on the state-of-the-art solutions in order to speed-up and optimize the operations.
- 2) Access to in situ data is a key for research development. Actually, UAS has the potential to collect dataset using sensors with similar characteristics of satellite multispectral sensors, with the advantages of strong flexibility in terms of geometry of acquisition, spatialization of the information, spatial resolution, and selection of the test sites. Moreover, UAS acquisition campaigns have cheap costs. The creation of accurate UAS dataset with high quality and high angular resolution features, and the definition of standard data processing and flight protocols for specific applications should be encouraged by space agencies in order to create integrated solutions to support and optimize the quality of satellite data products.
- 3) The UAS system has an intrinsic level of uncertainty coming from onboard sensors in charge of positioning (GPS, barometer, and compass) and sensor noise. These aspects have to be deeply evaluated in order to improve the data quality.
- 4) A fixed position of the Sun during the field campaigns has been assumed, although actually the Sun position varies

during the UAS acquisitions (the flight time for each field campaign was about 15 min), this leads to a degree of uncertainty in the data elaborations and, consequently, in the results.

D. Future Research Directions

- 1) UAS acquisitions over different surface types and under different illumination conditions.
- 2) The use of different BRDF models to fit the UAS measurements, such as nonlinear models with machine learning techniques.
- 3) Use of calibration panels for the radiometric correction of the data frame (made with the equipped ILS to date).
- 4) The UAS multispectral acquisition with an S2-like sensor (MAIA S2) can be exploited to investigate the following:
 - a) BRDF (or its approximation) modeling of several surfaces at high spatial resolution with new test sites;
 - b) calibration/validation activities on S2 data;
 - c) create a training dataset based on the UAS acquisition for artificial intelligence super-resolution algorithms dedicated to S2 data.
- 5) In situ absolute radiometric calibration of satellite sensors is usually done by measuring the field surface reflectance and atmospheric parameters while the satellite is passing over the calibration site. During the calibration process, surface reflectance measurement errors can be transferred to the calibration coefficients. For a satellite sensor with a large FOV, the surface reflectance error can be caused by the off-nadir angle of the sensor when observing the calibration site. The knowledge of the BRDF model for a surface plays a key role in solving the problem of the difference in viewing angle between satellite- and ground-based measurement data.

VII. CONCLUSION

In the context of the use of UAS for the BRDF modeling of target surface, the proposed work aims to pave the way in defining good practices for the collection of reference in situ validation dataset to improve and optimize the operational BRDF correction algorithms. This research addresses for the first time the issue of the angular geometry of the acquired observations and the related data processing approaches under specific experimental conditions. The most advanced collection measurement techniques by means of UAS are used to provide innovative acquisition methods, especially in terms of multiangular sampling capability of the area under investigation. This goes in the direction of tracing a path toward global guidelines for UAS-based surface reflectance products employed for BRDF modeling and, therefore, for calibration and validation activities of satellite missions with high spatial resolution. A point to be underlined is that the present research does not presume to provide a full compendium of rules to be strictly followed when dealing with BRDF characterization from UAS, but it is intended to offer recommendations in terms of UAS acquisition protocol and data elaboration techniques based on our experience, opening the way toward a standardization of the methods for BRDF retrieval by means of UAS.

Moreover, we are preparing to evaluate the performance of machine learning techniques for the BRDF modeling, and also the challenge of integrating measurements collected above other surface types is considered to set up a robust dataset for the inversion of different models.

ACKNOWLEDGMENT

The authors would like to thank Ph.D. Stefano Casadio for his support in giving useful directions and suggestions on the research activities.

REFERENCES

- [1] G. Schaepman-Strub, M. E. Schaepman, T. H. Painter, S. Dangel, and J. V. Martonchik, "Reflectance quantities in optical remote sensing—Definitions and case studies," *Remote Sens. Environ.*, vol. 103, no. 1, pp. 27–42, 2006.
- [2] J. G. Salomon, C. B. Schaaf, A. H. Strahler, F. Gao, and Y. Jin, "Validation of the MODIS bidirectional reflectance distribution function and albedo retrievals using combined observations from the aqua and terra platforms," *IEEE Trans. Geosci. Remote Sens.*, vol. 44, no. 6, pp. 1555–1565, Jun. 2006.
- [3] C. B. Schaaf et al., "First operational BRDF, albedo nadir reflectance products from MODIS," *Remote Sens. Environ.*, vol. 83, no. 1/2, pp. 135–148, 2002.
- [4] D. P. Roy et al., "A general method to normalize Landsat reflectance data to nadir BRDF adjusted reflectance," *Remote Sens. Environ.*, vol. 176, pp. 255–271, 2016.
- [5] J. V. Martonchik et al., "Determination of land and ocean reflective, radiative, and biophysical properties using multiangle imaging," *IEEE Trans. Geosci. Remote Sens.*, vol. 36, no. 4, pp. 1266–1281, Jul. 1998.
- [6] Q. Zhou, L. Tian, J. Li, and W. Li, "Assessment of bidirectional reflectance effects on desert and forest for radiometric cross-calibration of satellite sensors," *ISPRS J. Photogramm. Remote Sens.*, vol. 160, pp. 180–194, 2020.
- [7] N. Byford and C. A. Coburn, "Temporal variation in surface bidirectional reflectance of the railroad valley vicarious calibration test site in Nevada," *Can. J. Remote Sens.*, vol. 48, pp. 722–736, 2022.
- [8] W. A. Abdou et al., "Ground measurements of surface BRDF and HDRF using PARABOLA III," *J. Geophysical Res., Atmos.*, vol. 106, pp. 11967–11976, 2001.
- [9] Y. Jin et al., "Consistency of MODIS surface bidirectional reflectance distribution function and albedo retrievals: 2—Validation," *J. Geophysical Res., Atmos.*, vol. 108, 2003, Art. no. 4159.
- [10] Z. Wang et al., "Evaluation of MODIS albedo product (MCD43A) over grassland, agriculture and forest surface types during dormant and snow-covered periods," *Remote Sens. Environ.*, vol. 140, pp. 60–77, 2014.
- [11] K. Z. Doctor, C. M. Bachmann, D. J. Gray, M. J. Montes, and R. A. Fusina, "Wavelength dependence of the bidirectional reflectance distribution function (BRDF) of beach sands," *Appl. Opt.*, vol. 54, 2015, Art. no. F243.
- [12] Y. Yanjuan, Y. Guangjian, and W. Jindi, "The approach on leaf area index inversion using multiangular and multispectral data sets," *J. Remote Sens.*, vol. 6, pp. 117–122, 2005.
- [13] S. Jay et al., "Exploiting the centimeter resolution of UAV multispectral imagery to improve remote-sensing estimates of canopy structure and biochemistry in sugar beet crops," *Remote Sens. Environ.*, vol. 231, 2019, Art. no. 110898.
- [14] G. Singhal, B. Bansod, L. Mathew, J. Goswami, B. U. Choudhury, and P. L. N. Raju, "Estimation of leaf chlorophyll concentration in turmeric (*Curcuma longa*) using high-resolution unmanned aerial vehicle imagery based on kernel ridge regression," *J. Indian Soc. Remote Sens.*, vol. 47, no. 7, pp. 1111–1122, 2019.
- [15] P. P. J. Roosjen, B. Brede, J. M. Suomalainen, H. M. Bartholomeus, L. Kooistra, and J. G. P. W. Clevers, "Improved estimation of leaf area index and leaf chlorophyll content of a potato crop using multi-angle spectral data—Potential of unmanned aerial vehicle imagery," *Int. J. Appl. Earth Obs. Geoinf.*, vol. 66, pp. 14–26, 2018.
- [16] T. Hakala, J. Suomalainen, and J. I. Peltoniemi, "Acquisition of bidirectional reflectance factor dataset using a micro unmanned aerial vehicle and a consumer camera," *Remote Sens.*, vol. 2, pp. 819–832, 2010.

- [17] Z. H. Mao, L. Deng, F. Z. Duan, X. J. Li, and D. Y. Qiao, "Angle effects of vegetation indices and the influence on prediction of SPAD values in soybean and maize," *Int. J. Appl. Earth Observ. Geoinf.*, vol. 93, 2020, Art. no. 102198.
- [18] Z. Pan, H. Zhang, X. Min, and Z. Xu, "Vicarious calibration correction of large FOV sensor using BRDF model based on UAV angular spectrum measurements," *J. Appl. Remote Sens.*, vol. 14, no. 2, 2020, Art. no. 027501.
- [19] M. Kim, C. Jin, S. Lee, K.-M. Kim, J. Lim, and C. Choi, "Calibration of BRDF based on the field goniometer system using a UAV multispectral camera," *Sensors*, vol. 22, no. 19, Oct. 2022, Art. no. 7476.
- [20] J. J. M., J. R. Jimenez-perez, L. Padua, F. R. Feito, and J. J. Sousa, "An efficient method for acquisition of spectral BRDFs in real-world scenarios," *Comput. Graph.*, vol. 102, pp. 154–163, 2022.
- [21] E. Nocerino, M. Dubbini, F. Menna, F. Remondino, M. Gattelli, and D. Covi, "Geometric calibration and radiometric correction of the MAIA multispectral camera," *Int. Arch. Photogramm., Remote Sens. Spatial Inf. Sci.*, vol. 42, pp. 149–156, 2017.
- [22] A. Gatti and A. Bertolini, "Sentinel-2 products specification document," *Thales Alenia Space*, Cannes, France, Accessed: Feb. 23, 2015. [Online]. Available: <https://earth.esa.int/documents/247904/685211/Sentinel-2+Products+Specification+Document>
- [23] F. Maignan, F.-M. Bréon, and R. Lacaze, "Bidirectional reflectance of Earth targets: Evaluation of analytical models using a large set of spaceborne measurements with emphasis on the hot spot," *Remote Sens. Environ.*, vol. 90, no. 2, pp. 210–220, 2004.
- [24] W. Lucht, C. B. Schaaf, and A. H. Strahler, "An algorithm for the retrieval of albedo from space using semiempirical BRDF models," *IEEE Trans. Geosci. Remote Sens.*, vol. 38, no. 2, pp. 977–998, Mar. 2000.
- [25] G. Crucil, H. Zhang, K. Pauly, and K. Van Oost, "A semi-empirical anisotropy correction model for UAS-based multispectral images of bare soil," *Remote Sens.*, vol. 14, no. 3, 2022, Art. no. 537.
- [26] D. R. Myers, "Solar radiation resource assessment for renewable energy conversion," *Comprehensive Renewable Energy*, vol. 1, pp. 213–237, 2012.
- [27] W. Wanner, X. Li, and A. H. Strahler, "On the derivation of kernels for kernel-driven models of bidirectional reflectance," *J. Geophysical Res., Atmos.*, vol. 100, no. D10, pp. 21077–21089, 1995.
- [28] Z. Jiao et al., "A method for improving hotspot directional signatures in BRDF models used for MODIS," *Remote Sens. Environ.*, vol. 186, pp. 135–151, 2016.
- [29] X. Li and A. H. Strahler, "Geometric-optical bidirectional reflectance modeling of the discrete crown vegetation canopy: Effect of crown shape and mutual shadowing," *IEEE Trans. Geosci. Remote Sens.*, vol. 30, no. 2, pp. 276–292, Mar. 1992.
- [30] J. L. Roujean, M. Leroy, and P. Y. Deschamps, "A bidirectional reflectance model of the Earth's surface for the correction of remote sensing data," *J. Geophysical Res., Atmos.*, vol. 97, no. D18, pp. 20455–20468, 1992.
- [31] P. P. Roosjen, J. M. Suomalainen, H. M. Bartholomeus, and J. G. Clevers, "Hyperspectral reflectance anisotropy measurements using a pushbroom spectrometer on an unmanned aerial vehicle—Results for barley, winter wheat, and potato," *Remote Sens.*, vol. 8, no. 11, 2016, Art. no. 909.
- [32] J. Louis et al., "Sentinel-2 Sen2Cor: L2A processor for users," in *Proc. Living Planet Symp. Spacebooks Online*, 2016, pp. 1–8.
- [33] F. M. Bréon, F. Maignan, M. Leroy, and I. Grant, "Analysis of hot spot directional signatures measured from space," *J. Geophysical Res., Atmos.*, vol. 107, no. D16, 2002, Art. no. AAC-1.
- [34] H. Li, K. Yan, S. Gao, W. Song, and X. Mu, "Revisiting the performance of the kernel-driven BRDF model using filtered high-quality POLDER observations," *Forests*, vol. 13, 2022, Art. no. 435.



Ilaria Petracca (Member, IEEE) received the Laurea degree in environmental engineering (*cum laude*) in 2020 and the Ph.D. degree in computer science, control and geoinformation in 2024 from the Tor Vergata University of Rome, Rome, Italy, where she is currently a post-graduate research fellow.

From 2022 to 2023, she was a Visiting Student with Space Telecommunications, Astronomy and Radiation Laboratory, Department of Aeronautics and Astronautics, Massachusetts Institute of Technology, Cambridge, MA, USA. She works as an EO Data Scientist with GEO-K S.r.l., Rome, Italy. Her major research area includes volcanic ash detection and precipitation retrieval by means of neural networks and satellite data, and bidirectional reflectance distribution function characterization using unmanned aerial system.



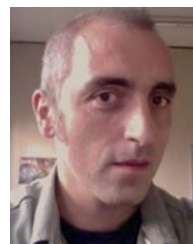
Daniele Latini received the Laurea degree in telecommunication engineering from the University of Rome "Tor Vergata," Rome, Italy, in 2010, and the Ph.D. degree in geoinformation from the Tor Vergata University of Rome, Rome, Italy, in 2015.

In 2013, he was a Visiting Student Researcher with Jet Propulsion Laboratory (JPL), California Institute of Technology, Pasadena, CA, USA, working on interferometric analysis using NASA UAVSAR data. In 2016, he obtained the license for UAV piloting in critical scenarios (A2 pilot licence). In 2020, he completed the post-Laurea master program "Design, Application, and Regulation of Unmanned Aerial Vehicle System (PARS)" with the University of Rome "Tor Vergata." Since 2010, he has been working in the field of remote sensing with Earth Observation Laboratory, Tor Vergata University, Rome, Italy, and then with its spin-off GEO-K. His activity is focused on the analysis of multispectral and synthetic aperture radar (SAR) remote sensing product, deeply investigating the ensemble of neural networks' techniques and architectures for a broad field of application, as well as on the integration of different technology solutions, such as artificial intelligence and on-board data processing. As a Project Manager, he has been responsible for several contracts funded by ESA, ASI, European Commission (HORIZON), and Italian Ministries (PRIN and PNRR), in the matter of EO products and services development in collaboration with various companies and research institutes. He was an External Professor with Tor Vergata University for the M.S. degree integrative course in "Microwaves." He has also been a Teacher in the "Postgraduate Master Program in "geoinformation and geographic information systems" with Tor Vergata University and he is the author of various publications in the field of Earth observation with multispectral and SAR data processing.



Marco Di Giacomo received the Laurea degree in ICT and Internet engineering (*cum laude*) in 2023 from the Tor Vergata University of Rome, Rome, Italy, where he is currently working toward the Ph.D. degree in computer science, control and geoinformation.

Since July 2022, he has been working as an Earth Observation Data Engineer with GEO-K S.r.l., Rome, Italy. His primary research areas include air quality, thunderstorm, and fog forecasting using machine learning approach and bidirectional reflectance distribution function characterization using unmanned aerial system.



Fabrizio Niro received the Ph.D. degree in physics from the University of Paris-Sud, Orsay, France, in 2003, specializing in molecular high-resolution spectroscopy and radiative transfer models in the thermal infrared domain.

He spent two years as a Visiting Scientist with the Department of Physical Chemistry, Bologna, working on retrieval methods for atmospheric remote sensing. Since 2005, he has been working with European Space Agency (ESA/ESRIN), based in Frascati, Italy, as a scientific and management Consultant for Serco,

Hook, U.K. He started as a remote sensing Specialist in support to algorithm development and calibration/validation (cal/val) activities for the MIPAS mission. In 2012, he was involved in cal/val preparatory activities for EarthCARE and Aeolus missions. Since 2015, he has been focusing his career on optical land imaging sensors, first as a remote sensing Expert and lead of the PROBA-V Quality Working Group, then as a Coordinator of various cross-cutting cal/val activities for land products validation. As a result, in April 2022, he was appointed as a Vice-Chair of the Land Products Validation Subgroup of the Committee on Earth Observation Satellites Working Group on cal/val.



Stefania Bonafoni (Senior Member, IEEE) received the Laurea (*cum laude*) and Ph.D. degrees in electronic engineering from the University of Perugia, Perugia, Italy, in 1997 and 2000, respectively.

Since 2005, she has been with the Department of Engineering, University of Perugia, where she teaches the class of remote sensing. Her research activity concerns the remote sensing of the Earth's atmosphere and surface: land surface temperature and albedo from satellite-based sensors; downscaling techniques for satellite images; microwave radiometry

from satellite and ground-based sensors for the estimation of atmospheric parameters; GPS for propagation delay and water vapor analyses; and GPS radio occultation for atmospheric profiling. She is an Associate Editor for the GRSS-IEEE Section of *IEEE Access* journal.



Fabio Del Frate (Senior Member, IEEE) received the Laurea degree in electronic engineering and the Ph.D. degree in computer science from the Tor Vergata University of Rome, Rome, Italy, in 1992 and 1997, respectively.

From 1995 to 1996, he was a Visiting Scientist with the Research Laboratory of Electronics, Massachusetts Institute of Technology, Cambridge, MA, USA. In 1998 and 1999, he was with ESRIN Centre, European Space Agency (ESA), Frascati. Since 1999, he has been with the University of Rome "Tor

Vergata," where he is currently a Full Professor, teaching courses on remote sensing and applied electromagnetism in various master's and Ph.D. programs. In the same university, he is also the Coordinator of the "Design, Application, and Regulation of UAVs" master program and Erasmus Coordinator for the engineering macroarea. In the framework of remote sensing educational international activities, he has been a Lecturer with different European Universities (Prague, Trier, and Cracow). He is, or has been, a Principal Investigator/Project Manager of several ESA and Italian Space Agency (ASI) funded research projects, an author of more than 200 international scientific publications, with a special focus on feature extraction algorithms from EO data using neural networks. In 2015, he was appointed by the European Organization for the Exploitation of Meteorological Satellites Associate Scientist for activities regarding the estimation of precipitation rate from satellite data. In 2019, he received an appointment by ESA as a Visiting Professor with ESA ESRIN Center to provide support in the use of artificial intelligence for Earth observation data processing. In 2006, he cofounded GEO-K srl, the first spin-off company of the University of "Tor Vergata" of which he is currently the President. He has been an Associate Editor for the journal *IEEE Geoscience and Remote Sensing*.

Open Access funding provided by 'Università degli Studi di Roma "Tor Vergata"' within the CRUI CARE Agreement